

Dependence of the electronic structure of self-assembled (In , Ga) As / Ga As quantum dots on height and composition

Gustavo A. Narvaez, Gabriel Bester, and Alex Zunger

Citation: *Journal of Applied Physics* **98**, 043708 (2005); doi: 10.1063/1.1980534

View online: <http://dx.doi.org/10.1063/1.1980534>

View Table of Contents: <http://scitation.aip.org/content/aip/journal/jap/98/4?ver=pdfcov>

Published by the [AIP Publishing](#)

Articles you may be interested in

[Polarization dependence of absorption by bound electrons in self-assembled quantum dots](#)
J. Appl. Phys. **113**, 193102 (2013); 10.1063/1.4805061

[Spontaneous localization in InAs/GaAs self-assembled quantum-dot molecules](#)
Appl. Phys. Lett. **81**, 4449 (2002); 10.1063/1.1526167

[Simulated self-assembly and optoelectronic properties of InAs/GaAs quantum dot arrays](#)
J. Appl. Phys. **92**, 4653 (2002); 10.1063/1.1505687

[Interband transition distributions in the optical spectra of InAs/GaAs self-assembled quantum dots](#)
Appl. Phys. Lett. **80**, 2755 (2002); 10.1063/1.1469214

[Composition, volume, and aspect ratio dependence of the strain distribution, band lineups and electron effective masses in self-assembled pyramidal In_{1-x}Ga_xAs/GaAs and Si_xGe_{1-x}/Si quantum dots](#)
J. Appl. Phys. **91**, 389 (2002); 10.1063/1.1410318



Frustrated by old technology? Is your AFM dead and can't be repaired? Sick of bad customer support?

It is time to upgrade your AFM
Minimum \$20,000 trade-in discount for purchases before August 31st

Asylum Research is today's technology leader in AFM

dropmyoldAFM@oxinst.com

OXFORD INSTRUMENTS
The Business of Science®

Dependence of the electronic structure of self-assembled (In,Ga)As/GaAs quantum dots on height and composition

Gustavo A. Narvaez, Gabriel Bester, and Alex Zunger^{a)}

National Renewable Energy Laboratory, Golden, Colorado 80401

(Received 15 February 2005; accepted 27 May 2005; published online 23 August 2005)

While electronic and spectroscopic properties of self-assembled $\text{In}_{1-x}\text{Ga}_x\text{As}/\text{GaAs}$ dots depend on their shape, height, and alloy compositions, these characteristics are often not known accurately from experiment. This creates a difficulty in comparing measured electronic and spectroscopic properties with calculated ones. Since simplified theoretical models (effective mass, $\mathbf{k}\cdot\mathbf{p}$, parabolic models) do not fully convey the effects of shape, size, and composition on the electronic and spectroscopic properties, we offer to bridge the gap by providing accurately calculated results as a function of the dot height and composition. Prominent features of our results are the following: (i) Regardless of height and composition, the confined electron energy levels form shells of nearly degenerate states with a predominant s, p, \dots orbital character. On the contrary, the confined hole energy levels form shells only in flat dots and near the highest hole level (HOMO). (ii) In alloy dots, the *electrons* s - p splitting depends weakly on height, while the p - p splitting depends nonmonotonically due to alloy fluctuations. In pure, nonalloyed InAs/GaAs dots, *both* these splittings depend weakly on height. Furthermore, the s - p splitting is larger, while the p - p has nearly the same magnitude. For *hole* levels in alloy dots, the s - p splitting decreases with increasing height (the splitting in tall dots being about four times smaller than in flat dots), whereas the p - p splitting remains nearly unchanged. Shallow, pure, nonalloyed dots have a s - p splitting of nearly the same magnitude, whereas the p - p splitting is about three times larger. (iii) As height increases, the s and p characters of the wave function of the HOMO becomes mixed, and so does its heavy-hole and light-hole characters. (iv) In alloy dots, regardless of height, the wave function of low-lying hole states are localized inside the dot. Remarkably, in nonalloyed InAs/GaAs dots these states become localized at the interface as height increases. The localized states are nearly degenerate and polarized along $[1\bar{1}0]$ and $[110]$. This localization is driven by the peculiarities of the biaxial strain present in the nanostructure. © 2005 American Institute of Physics.

[DOI: 10.1063/1.1980534]

I. INTRODUCTION

The electronic structure and spectroscopic properties of quantum dots, including excitons,^{1–6} charged excitons,^{2,3} multiexcitons,^{3–5} and excitonic fine structure,⁶ all depend on the size and shape of the dots. This dependence reflects both quantum confinement effects, as well as shape-induced band folding and interband coupling.⁷ Simulations of the electronic structure and spectroscopic properties of quantum dots^{8–14} must naturally assume the size and shape of the dot. On the other hand, *measurements* of the spectroscopic properties of a dot^{1–6} are rarely accompanied by accurate measurements of the size and shape of the GaAs-covered dot, except in rare cases where detailed cross-sectional scanning tunneling microscopy experiments are performed, such as in Refs. 15–17. This situation creates a significant difficulty, if not a crisis, in interpreting spectroscopic data on quantum dots and in critically testing various theoretical approaches. Thus, in reality one is often forced to address the inverse problem,¹³ namely, fit the spectroscopic data to a theoretical model by using the size and shape as adjustable parameters. The difficulty with this approach is threefold: First, in this

approach all theories, no matter how naïve, ultimately work by virtue of forcing a fit to experiment, even if the assumptions entering the theory may seem unjustified in their own right (e.g., assumption of a single-band effective mass, neglect of strain, neglect of spin-orbit coupling.) Second, there are usually too many free parameters, which involve not only nontrivial shapes, but also unknown composition profiles (e.g., $\text{In}_{1-x}\text{Ga}_x\text{As}$ dots). Third, since the relationship between shape and spectroscopic properties is model dependent, unrealistic shapes are often deduced. For example, in simple effective mass,^{12,18–20} $\mathbf{k}\cdot\mathbf{p}$ or parabolic models the p and d levels of electrons and holes are degenerate if one assumes spherical, lens-shaped, cubic, or cylindrical dots. On the contrary, in more advanced *atomistic* models—like empirical pseudopotential^{21–23} or tight binding²⁴—those levels are split even for the above-mentioned ideal shapes, resulting in clear spectroscopic signatures. To fit measured spectroscopic signatures of actual dots by simple theoretical models, one needs to assume at the outset irregular shapes. For instance, Dekel *et al.*⁵ needed to assume a parallelepipedal box to explain their multiexciton data on nonalloyed InAs/GaAs dots, and Ferreira assumed shape distortions to explain fine structure.²⁵ Such assumptions are not needed in atomistic approaches to modeling.

^{a)}Electronic mail: alex_zunger@nrel.gov

In this work we have used a high-level atomistic approach to predict the spectroscopic characteristics of $\text{In}_{1-x}\text{Ga}_x\text{As}/\text{GaAs}$ self-assembled dots as functions of the most crucial geometric parameter, namely, the height. We calculate strain profiles, p - and d -level splittings, as well as electron and hole wave functions. While ultimately it will be necessary for experimentalists to report the size, shape, and composition profiles to which their spectroscopic data correspond, the type of study reported here may be used to bridge, in the interim, spectroscopy with theory without clouding the issue by severe theoretical approximations.

Similar studies have been carried out previously and can be divided into two groups: (a) calculations that used the $\mathbf{k}\cdot\mathbf{p}$ method^{26–30} and (b) calculations that adopted the present atomistic pseudopotential approach.^{13,14,31} These two methods have been compared by Wang *et al.*²² The series of papers in (a), as well as Ref. 31, focused on *pyramid-shaped* nonalloyed InAs/GaAs quantum dots, while here we treat more realistic lens-shaped, alloyed $\text{In}_{1-x}\text{Ga}_x\text{As}/\text{GaAs}$ dots. Studies in group (a) addressed the effects of the dot base and height size on the single-particle electronic structure and optical properties,^{26–29} as well as on many-particle exciton and biexciton states.³⁰ Regarding group (b) of atomistic pseudopotential calculations, the work of Shumway *et al.*¹³ considered a *truncated-pyramid* model of $\text{In}_{1-x}\text{Ga}_x\text{As}/\text{GaAs}$ quantum dots that produced the best agreement between theoretical predictions and data on electronic and optical properties. These authors addressed the effect of varying the In concentration in the dot, as well as the In concentration profile within the dot. On the other hand, Williamson, Wang, and Zunger¹⁴ also used the pseudopotential method to address the electronic structure and optical properties of lens-shaped $\text{In}_{1-x}\text{Ga}_x\text{As}/\text{GaAs}$ quantum dots and compared their results with available data. Williamson *et al.*¹⁴ focused on flat dots (with heights of 25 and 35 Å) while addressing primarily the effect of In concentration profile within the dot. Finally, Kim, Wang, and Zunger³¹ used the pseudopotential method to compare the single-particle electronic structure of pyramid-shaped, nonalloyed InAs/GaAs dots with different facet orientations ([101], [113], and [105]). The latter naturally led to dots with different height-to-base ratios for the base sizes (90 and 113 Å) chosen by Kim, Wang, and Zunger.

II. METHODS AND THEIR ILLUSTRATION

A. Choice of dot geometries

Among several geometries, Stranski-Krastanow quantum dots grow in lens shape.³² Hence, we focus on lens-shaped, self-assembled $\text{In}_{1-x}\text{Ga}_x\text{As}/\text{GaAs}$ quantum dots (QDs). In addition, we include a one-monolayer-thick $\text{In}_{1-x}\text{Ga}_x\text{As}$ wetting layer (WL). Figure 1 shows a sketch of the geometry of the nanostructure. (QD+WL+GaAs matrix). We focus on dots with $x=0.4$ and pure InAs . The QDs have circular base with diameter $b=252$ Å and height h in the interval of 20–75 Å.

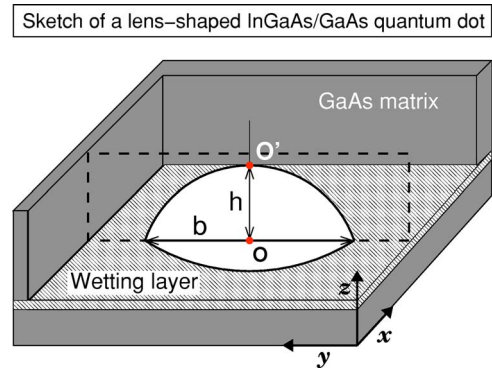


FIG. 1. (Color online) Sketch of the geometry of self-assembled $\text{In}_{1-x}\text{Ga}_x\text{As}/\text{GaAs}$ quantum dots. A section of the GaAs matrix (grey) has been omitted for clarity. The dot (white) is lens shaped with base diameter b and height h . The dot lies on top of a one-monolayer-thick $\text{In}_{1-x}\text{Ga}_x\text{As}$ wetting layer. Two auxiliary features are shown: (i) A plane that bisects the dot (dashed lines) and (ii) the line $\overline{OO'}$, which pierces the dot through the center along the [001] direction.

B. Strain relaxation done via atomistic elasticity instead of continuum elasticity

The position-dependent strain profiles present in the nanostructure are usually addressed within the (harmonic) *continuum* elasticity (CE) theory.^{33,34} Nevertheless, strain profiles can also be calculated within atomistic elasticity (AE) in the form of a valence force field.³⁵ In AE the strain energy is expressed in terms of atomic positions and interatomic force constants. While the force constants are fit to the elastic constants C_{11} , C_{12} , and C_{44} , much like in CE, expressing the strain in terms of atomic positions contains much more information than expressing strain in terms of CE coordinates. For example, a square-based pyramid has a C_{4v} point group symmetry if described by CE. This means that the [110] and $[\bar{1}\bar{1}0]$ facets are taken to be equivalent. In this case, all p energy levels are degenerate. However, in AE the point-group symmetry of a square-based pyramid made of InAs is C_{2v} . In this case, the [110] and $[\bar{1}\bar{1}0]$ facets are symmetry-inequivalent and p levels are split. In general, three interrelated sources are responsible for the splitting of the p states.³⁶ A quantum dot with a base that globally possesses inversion symmetry in the (001) plane—like a lens, a truncated pyramid, or a truncated cone—has in reality the lower C_{2v} symmetry (for pure, nonalloyed InAs/GaAs dots), which originates from the underlying zinc-blende atomic lattice. Thus, the *first source* is the lack of inversion symmetry in the C_{2v} point group, which manifests itself around the dot-matrix interfaces where the [110] and $[\bar{1}\bar{1}0]$ directions are inequivalent. The *second source* is the propagation of the strain field towards the center the dot as a consequence of the atomic relaxation. The *third source* is the piezoelectric effect (which magnitude is presently under debate³⁶) that arises from the strain field of the C_{2v} symmetry. It should be noted that approximations used in previous calculations of the piezoelectric effect^{37,38} have been shown to be crude, and further investigations have been called for.³⁶

Our choice of AE is based on a generalization of the Keating model to three terms—bond-bending, bond-stretching, and their cross terms.¹⁴ We fit the elastic constants

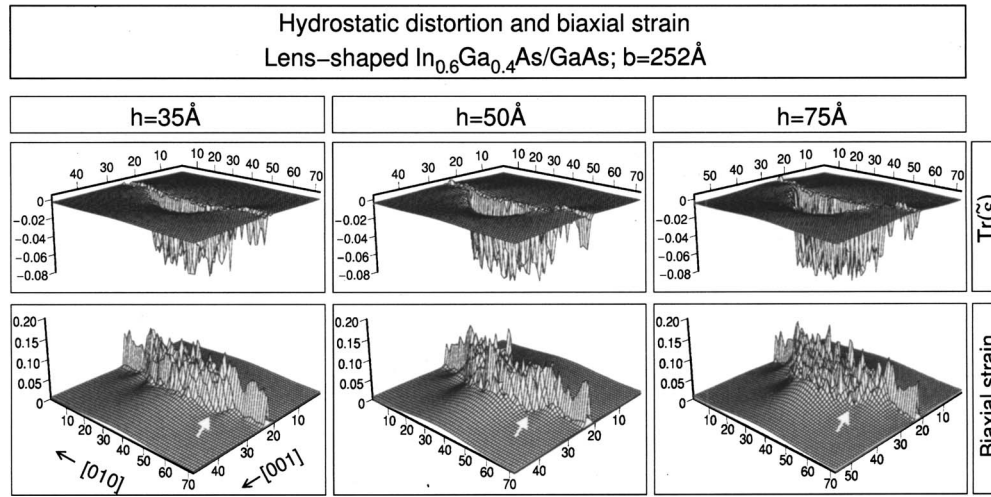


FIG. 2. Hydrostatic distortion [$\text{Tr}(\bar{\epsilon})$; top] and biaxial strain (bottom) as functions of dot height plotted on a planar section that is normal to $[100]$ and bisects the dot (see Fig. 1). Positions are measured in units of $a_{\text{GaAs}} = 5.65 \text{ \AA}$. The wetting-layer (WL) strain appears prominently. Alloy fluctuations make the strain profiles sample dependent. Two robust features emerge: (i) The biaxial strain at the top of the dot increases with height and slowly decays off. The taller the dot the faster this decays. $\text{Tr}(\bar{\epsilon})$ shows a similar trend. (ii) The underlying zinc-blende atomic structure causes the strain to rapidly drop to zero along the $[011]$ and $[01\bar{1}]$ directions. Arrows indicate this feature.

C_{11} , C_{12} , and C_{44} of zinc-blende InAs and GaAs, as well as the correct dependence of the Young modulus with pressure for both materials. In the $\text{In}_{1-x}\text{Ga}_x\text{As}$ alloy system, the bond-stretching and the bond-stretching/bond-bending cross-term parameters for the mixed cation Ga–As–In bond angle are taken as the algebraic average of the In–As–In and Ga–As–Ga values. While the ideal bond angle is 109° for the pure zinc-blende crystal, to satisfy Vegard's law for the alloy volume, the value of 110.5° was used for the mixed bond angle. AE is superior to CE in that it does not assume harmonicity; in fact, anharmonic effects can be explicitly included³⁹ into the valence force field.³⁵

Here, we calculate the position-dependent strain tensor $\bar{\epsilon}(\mathbf{R})$ within the atomistic elasticity approach. To calculate the strain tensor cubic components ϵ_{ij} ($i, j = x, y, z$), we proceed in two steps: (1) We relax the atomic positions within the supercell in order to minimize the elastic energy, which is given by a generalized valence force field.¹⁴ (2) We relate the relaxed (equilibrium) atomic positions with the unrelaxed atomic positions via strain tensor.³⁴ At each equilibrium position \mathbf{R}_l of atom l we identify the tetrahedron formed by its four nearest neighbors. This tetrahedron is distorted in comparison to the unrelaxed tetrahedron. Thus, the three edges of these tetrahedra that are determined by the vectors connecting the four neighbors can be related by the strain tensor $\bar{\epsilon}$ as follows:

$$\begin{pmatrix} \mathbf{R}_{al,x} & \mathbf{R}_{bl,x} & \mathbf{R}_{cl,x} \\ \mathbf{R}_{al,y} & \mathbf{R}_{bl,y} & \mathbf{R}_{cl,y} \\ \mathbf{R}_{al,z} & \mathbf{R}_{bl,z} & \mathbf{R}_{cl,z} \end{pmatrix} = \begin{pmatrix} 1 + \epsilon_{xx} & \epsilon_{yx} & \epsilon_{zx} \\ \epsilon_{xy} & 1 + \epsilon_{yy} & \epsilon_{zy} \\ \epsilon_{xz} & \epsilon_{yz} & 1 + \epsilon_{zz} \end{pmatrix} \times \begin{pmatrix} \mathbf{R}_{al,x}^0 & \mathbf{R}_{bl,x}^0 & \mathbf{R}_{cl,x}^0 \\ \mathbf{R}_{al,y}^0 & \mathbf{R}_{bl,y}^0 & \mathbf{R}_{cl,y}^0 \\ \mathbf{R}_{al,z}^0 & \mathbf{R}_{bl,z}^0 & \mathbf{R}_{cl,z}^0 \end{pmatrix}, \quad (1)$$

where \mathbf{R}_{al} , \mathbf{R}_{bl} , and \mathbf{R}_{cl} are the three vectors that connect, respectively, neighbors 1 and 2, 2 and 3, and 3 and 4 in the

equilibrium-distorted tetrahedron that encloses atom l . \mathbf{R}_{al}^0 , \mathbf{R}_{bl}^0 , and \mathbf{R}_{cl}^0 are the corresponding vectors (edges) in the unrelaxed tetrahedron. From Eq. (1), the cubic strain tensor components are calculated by a matrix inversion.

Figure 2 shows the biaxial strain

$$B = \sqrt{(\epsilon_{xx} - \epsilon_{yy})^2 + (\epsilon_{yy} - \epsilon_{zz})^2 + (\epsilon_{zz} - \epsilon_{xx})^2} \quad (2)$$

and the hydrostatic distortion (isotropic strain) $I = \text{Tr}(\bar{\epsilon})$ as a function of dot height. The results presented correspond to the strain values on a planar section in the $[100]$ direction that bisects the dot (see Fig. 1). The spikes in the dot and wetting-layer region are a consequence of the random arrangement of In and Ga atoms. Thus, the spikes structure significantly changes from dot to dot. Two additional features are also prominent. (i) The biaxial strain at the dot-matrix interface, located near the top of the dot, increases with height and slowly decays off. This decay is faster as the dot becomes taller. The latter can be understood by considering the dot as a spherical cap inscribed in a sphere of radius $\rho_0 = [h^2 + (b/2)^2]/2h$ (the taller the dot, the smaller ρ_0) and by assuming that the decay of B outside the dot is qualitatively well described by $(\rho_0/\rho)^3$, which is the radial dependence of the biaxial strain outside a continuum, elastic sphere of radius ρ_0 embedded in a lattice-mismatched medium.⁴⁰ Here, ρ is the radial distance from the sphere surface. In our simulations, $\text{Tr}(\bar{\epsilon})$ shows a trend similar to that of B . (ii) Due to the underlying zinc-blende atomic structure, the biaxial strain drops to zero along the $[011]$ and $[01\bar{1}]$ directions, as well as along their equivalent crystallographic directions. (See white arrows in Fig. 2.) This feature is robust upon changes in height, being present for all the quantum dots we considered.

C. The single-particle electronic structure is calculated via the pseudopotential plane-wave method instead of the k-p method

To calculate the energies and wave functions of electron and hole states in the quantum dot, we use the empirical

pseudopotential method of Wang and Zunger.²¹ This approach combines a pseudopotential description of the single-particle Hamiltonian with the linear combination of bulk bands (LCBB) method to solve for the energies and wave functions.²¹ In this method, the Hamiltonian reads

$$\mathcal{H} = -\frac{\beta}{2}\nabla^2 + V_{\text{SO}} + \sum_{\alpha=\text{In,Ga,As}} \sum_l v_{\alpha}(\mathbf{R} - \mathbf{R}_l^{\alpha}; \bar{\varepsilon}), \quad (3)$$

where β is an empirical parameter that accounts for nonlocality effects, V_{SO} is a nonlocal empirical operator that describes the spin-orbit interaction;¹⁴ $v_{\alpha}(\eta; \bar{\varepsilon})$ is a screened pseudopotential (for atom of type α) that depends on strain; and \mathbf{R}_l^{α} is the relaxed vector position of atom l of type α . The dependence of the atomic pseudopotential on strain transfers to the electronic Hamiltonian the information on atomic displacements. The strain-dependent pseudopotential reads

$$v_{\alpha}(\mathbf{R} - \mathbf{R}_l^{\alpha}; 0)[1 + \gamma_{\alpha} \text{Tr}(\bar{\varepsilon})], \quad (4)$$

where γ_{α} is a fitting parameter. It should be noted that $v_{\alpha}(\mathbf{R} - \mathbf{R}_l^{\alpha}; \bar{\varepsilon})$ is fit to *bulk* properties of GaAs and InAs, including bulk band structures, experimental deformation potentials, and effective masses, and local-density approximation-determined band offsets. In order to improve the transferability of pseudopotential $v_{\alpha}(\mathbf{R} - \mathbf{R}_l^{\alpha}; \bar{\varepsilon})$, a simple dependence on the chemical environment of atom α is introduced. For instance, for $\alpha=\text{As}$ in an environment of p Ga atoms and $p-4$ In atoms we use

$$v_{\text{As}}^{(p)} = \frac{(4-p)}{p} v_{\text{As}}(\text{InAs}) + \frac{p}{r} v_{\text{As}}(\text{GaAs}). \quad (5)$$

The pseudopotentials used in this work have been successfully tested for quantum wells.¹⁴

The wave function $\psi_i(\mathbf{R})$ of state i , which satisfies $\mathcal{H}\psi_i = \mathcal{E}_i\psi_i$, is expanded in bulk Bloch states $u_{n,k}^{(M)}(\mathbf{R})$ of material M . [It should be noted that the bulk materials (M) can be strained.²¹] Namely,

$$\psi_i(\mathbf{R}) = \sum_M \sum_{n,\mathbf{k}} C_{M;n,\mathbf{k}}^{(i)} \left[\frac{1}{\sqrt{N}} u_{n,\mathbf{k}}^{(M)}(\mathbf{R}) e^{i\mathbf{k}\cdot\mathbf{R}} \right], \quad (6)$$

where n and \mathbf{k} indicate the band index and wave vector of the Bloch state, respectively, and N is the number of primary cells contained in a supercell that encloses the quantum dot. Thus, by diagonalizing the Hamiltonian [Eq. (3)] in the Bloch states basis we find the coefficients $C_{M;n,\mathbf{k}}^{(i)}$. The calculated wave functions $\psi_i(\mathbf{R})$ are two-fold Kramers degenerate, so we have omitted the spin index σ . This representation for the wave function is very different from the familiar $\mathbf{k}\cdot\mathbf{p}$ method in that in the latter approach the basis set is constructed only from states near the Brillouin zone center (Γ), while here we use a full-zone description. Further, in $\mathbf{k}\cdot\mathbf{p}$ one is restricted to just one or two Bloch bands at Γ (8×8 representing two Bloch bands), while here we consider n Bloch bands. In the Appendix, we present an assessment of the convergence of energy levels \mathcal{E}_i as a function of the expansion parameters in Eq. (6).

D. Strain-modified band offsets

While we describe the effects of strain on the electronic structure atomistically, as shown in Eq. (3), here, for *illustrative purposes only*, we calculate the conduction (electron) and valence (hole) strain-modified band offsets (confining potentials) present in the quantum dot by coupling strain to $\mathbf{k}\cdot\mathbf{p}$ -like equations. At each eight-atom unit cell in the supercell we diagonalize the conduction and valence (including spin-orbit coupling) band strain Hamiltonians that Wei and Zunger put forward in Ref. 41. Figure 3 shows the calculated strain-modified band offsets for electrons and holes along the line $\overline{OO'}$ indicated in Fig. 1. The electron band offset appears in the upper panel, whereas thick and thin lines in the lower panel show the first and second hole offsets, respectively. We note the following features. (i) The band offsets (Fig. 3) inherit the jagged nature of the strain fields (Fig. 2). Inside the quantum dot (region D in Fig. 3), alloy fluctuations lead to a small mixing in the heavy-hole (HH) and light-hole (LH) characters of the band offsets. (ii) Regardless of the dot height, the higher-energy hole band offset has a HH character inside the dot and a LH one outside. Conversely, the lower-energy hole band offset has a LH character inside and a HH one outside. (iii) The increase in biaxial strain at the dot-matrix interface that occurs as the height increases (Fig. 2) is reflected in the increase (decrease) of the higher (lower)-energy hole band offset. (See arrows in Fig. 3). In particular, for tall dots, the decrease of the lower-energy hole offset at the interface leads to the formation of a *pocket* in the band offset.

E. Orbital and Bloch character of wave functions

The single-band effective-mass model predicts that in the continuum limit, in which lens-shaped dots have full axial symmetry, the confined energy levels will form shells of degenerate states with *definite* angular momentum $l = 0, 1, 2, \dots$ (Ref. 42). Thus, the *orbital* character of the confined levels will be *pure* s , p , d , etc. However, when the correct symmetry of the dot is taken into account, as it is the case when using our atomistic pseudopotential method, the confined energy levels can have a mixed orbital character. To quantify the degree of mixing, we analyze the single-particle wave functions $\psi_i(\mathbf{R})$ by projecting their *envelopes* on eigenfunctions of the axial ($\parallel z$; see Fig. 1) angular momentum $e^{im\phi}/\sqrt{2\pi}$ and determine the orbital (angular) character. The latter is given by

$$A_{m,n}^{(i)} = \int dz \int d\rho \rho \left| \int d\phi f_n^{(i)}(\rho, \phi, z) \frac{e^{im\phi}}{\sqrt{2\pi}} \right|^2. \quad (7)$$

In Eq. (7), we have used cylindrical coordinates, i.e., $\mathbf{R} = (\rho, \phi, z)$, and have written the Γ -derived envelope function as

$$f_n^{(i)}(\rho, \phi, z) = \sum_M \sum_{\mathbf{k}} \sum_{n'} C_{M;n,\mathbf{k}}^{(i)} \langle u_{n,\mathbf{k}}^{(M)} | u_{n',\Gamma}^{(M)} \rangle \frac{e^{i\mathbf{k}\cdot\mathbf{R}}}{\sqrt{N}}. \quad (8)$$

The Bloch character of the hole wave functions $\psi_i^{(h)}$ in the quantum dot depends on strain as well as on band coupling. To study the extent to which the Bloch character is

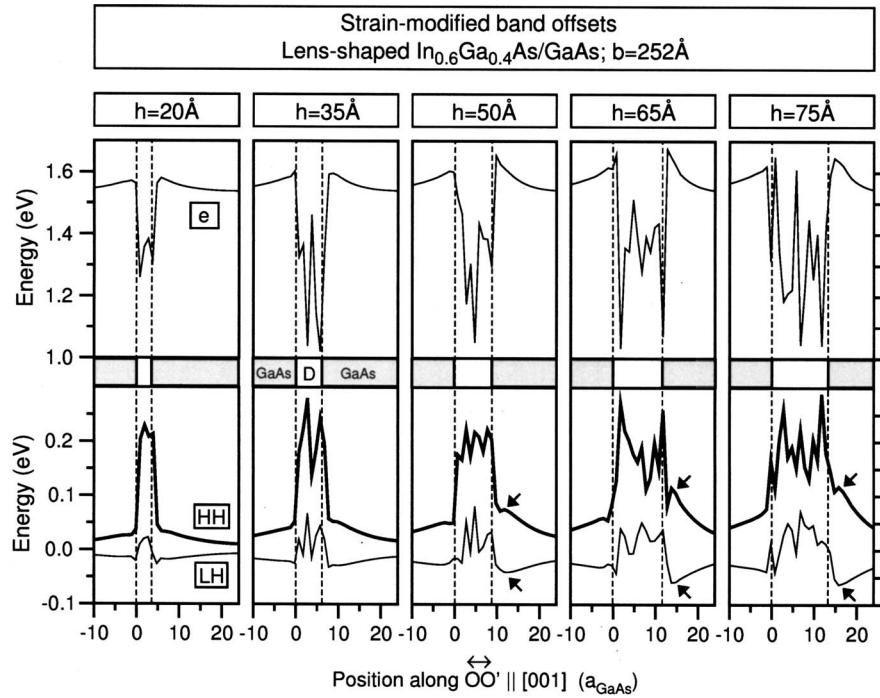


FIG. 3. Strain-modified band offsets for electrons (upper panel, e) and first and second holes (lower panel; thick and thin lines, respectively) along the $\overline{OO'} \parallel [001]$ as functions of height. (See Fig. 1.) In the dot region (indicated with a D) the offsets are irregular (jagged) due to alloy fluctuations. These irregularities are more noticeable as the height increases. Outside D the heavy-hole (HH) and light-hole (LH) characters reverse. Arrows indicate “pocket” formation in the second hole band offset as the dot height increases.

HH, LH, and SO, we proceed similarly and project the envelope of $\psi_i^{(h)}(\mathbf{R})$ on the total angular momentum basis $|J, J_z\rangle$ ($\{|3/2, \pm 3/2\rangle, |3/2, \pm 1/2\rangle, |1/2, \pm 1/2\rangle\}$).

F. Exciton energy levels are obtained via the screened configuration-interaction approach, not via perturbation theory

We calculate the exciton energy levels E_ν by using the configuration-interaction (CI) method as proposed in Ref. 43. Briefly, in this method, the exciton states

$$\Psi_\nu = \sum_{i,j} C_{ij}^{(\nu)} |e_i h_j\rangle, \quad (9)$$

where $\{|e_i h_j\rangle\}$ denotes a basis of single-substitution Slater determinants (configurations), in which an electron is promoted from $\psi_j^{(h)}(\mathbf{R})$ to $\psi_i^{(e)}(\mathbf{R})$. The CI method would deliver the exact exciton ground and excited states in the case of a complete basis. However, we *truncate* this basis and consider all the possible configurations build out of n_e electron and n_h hole confined states. The coefficients $C_{ij}^{(\nu)}$ arise from the diagonalization of the exciton Hamiltonian. The direct $[J_{ij} = J_{ij,ji}^{(eh)}]$ and exchange $[K_{ij} = K_{ij,ij}^{(eh)}]$ electron-hole Coulomb integrals that enter the calculation are derived from the electron-hole Coulomb and exchange-scattering matrix elements:

$$J_{ij,kl}^{(eh)} = \iint d\mathbf{R} d\mathbf{R}' \frac{[\psi_i^{(h)}(\mathbf{R})]^* [\psi_j^{(e)}(\mathbf{R}')]^* [\psi_k^{(e)}(\mathbf{R}')] [\psi_l^{(h)}(\mathbf{R})]}{\epsilon(\mathbf{R}, \mathbf{R}') |\mathbf{R} - \mathbf{R}'|}, \quad (10)$$

$$K_{ij,kl}^{(eh)} = \iint d\mathbf{R} d\mathbf{R}' \frac{[\psi_i^{(h)}(\mathbf{R})]^* [\psi_j^{(e)}(\mathbf{R}')]^* [\psi_k^{(e)}(\mathbf{R})] [\psi_l^{(h)}(\mathbf{R}')] }{\epsilon(\mathbf{R}, \mathbf{R}') |\mathbf{R} - \mathbf{R}'|}. \quad (11)$$

The microscopic, phenomenological dielectric constant $\epsilon(\mathbf{R}, \mathbf{R}')$ that screens the interaction is calculated within the Thomas-Fermi model proposed by Resta.⁴⁴ We do not use simple perturbation theory where the exciton is described via a Coulomb-corrected single-particle band gap ($\mathcal{E}_i^e - \mathcal{E}_j^h - J_{ij}$; here, \mathcal{E}_i^e and \mathcal{E}_j^h are the energies of electron level i and hole level j , respectively).

III. RESULTS

We now present the effects of height and composition on the energies of confined levels and their splittings, wave functions of selected confined electron and hole levels, and the lowest transition energy of the exciton.

A. Energies of confined levels: p levels are split even for ideal lens-shape dots

The confined electron and hole energy levels are respectively labeled as \mathcal{E}_i^e and \mathcal{E}_i^h , where $i=0, 1, \dots$ is an orbital quantum number. The corresponding wave functions are $\psi_n^{(e)}(\mathbf{r})$ and $\psi_n^{(h)}(\mathbf{r})$. Each of the confined states are twofold, Kramers degenerate. We label the $i=0$ electron and hole states as LUMO and HOMO, respectively. The first 20 electron and hole energy levels of an $\text{In}_{0.6}\text{Ga}_{0.4}\text{As}/\text{GaAs}$ dot appear in Fig. 4. The electron and hole energies are measured, respectively, from the bottom of the conduction band (CBM) $E_c(\text{GaAs}) = -4.093$ eV (calculated bulk electron affinity) and from the top of the valence band (VBM) $E_v(\text{GaAs}) =$

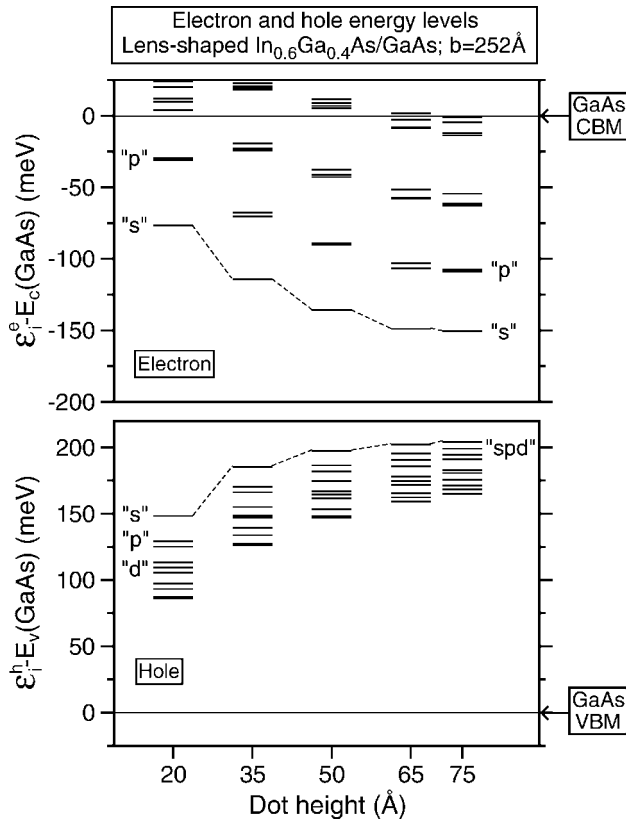


FIG. 4. First 20 electron (top panel) and hole (bottom) energy levels \mathcal{E}_n^e and \mathcal{E}_n^h for $\text{In}_{0.6}\text{Ga}_{0.4}\text{As}/\text{GaAs}$ dots with different heights. The electron and hole energies are measured from GaAs CBM [$E_c(\text{GaAs}) = -4.093$ eV] and GaAs VBM [$E_v(\text{GaAs}) = -5.620$ eV], respectively. As height increases, the number of confined levels ($\mathcal{E}_n^e < 0$ and $\mathcal{E}_n^h > 0$) increases and the single-particle gap ($\mathcal{E}_0^e - \mathcal{E}_0^h$) decreases. The confined electronic energy levels group in *non-degenerate shells* for all dots. *s*, *p*, and *d* indicate the predominant orbital character of selected states. For holes, up to $h = 50$ Å the second and third levels are *p*-like, while for larger heights these levels are *s-p* hybridized.

-5.620 eV (calculated bulk ionization potential) of bulk GaAs. For all heights, the confined electron states form groups (*shells*) of *nondegenerate* levels.⁴⁴ In turn, this shell structure can only be identified for the first few hole levels (near HOMO) in shallow dots (up to $h = 50$ Å). For taller dots, the holes show no shell structure. The number of confined electron states is significantly smaller than that of holes. While for the tallest dot there are ten confined electron states, more than 150 hole states are confined in all the considered dots. When comparing the results for $h = 35$ Å with the first 20 electron and hole energy levels (not shown) in a lens-shaped, nonalloyed InAs/GaAs dot, we find that (i) the electron levels form shells that have a bigger average separation (55 vs 45 meV in $\text{In}_{0.6}\text{Ga}_{0.4}\text{As}/\text{GaAs}$), (ii) the hole energy-level structure near the HOMO is significantly different (see splittings in Fig. 5), and (iii) the single-particle gap $\mathcal{E}_0^e - \mathcal{E}_0^h$ is smaller (see Fig. 10).

Energy splittings

The *s-p* energy splitting $\mathcal{E}_1 - \mathcal{E}_0$ and *p-p* splitting $\mathcal{E}_2 - \mathcal{E}_1$ for electrons and holes are shown in Fig. 5 as a function of the dot height. (The dots' single-particle gap is also indicated.) Two features emerge. First, *s-p* splitting for electrons is bigger than for holes. For electrons, the magnitude of the

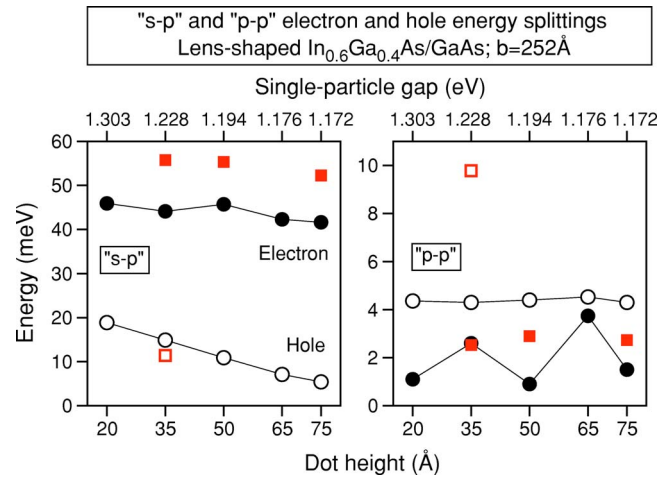


FIG. 5. (Color online) Height dependence of the *s-p* ($\mathcal{E}_1 - \mathcal{E}_0$) and *p-p* ($\mathcal{E}_2 - \mathcal{E}_1$) energy splittings for electron and hole levels in $\text{In}_{0.6}\text{Ga}_{0.4}\text{As}/\text{GaAs}$. The single-particle gap is also shown. The *s-p* splitting for electrons is bigger than for holes; in turn, the *p-p* splitting shows the opposite trend. The height dependence of the *p-p* splitting for electrons is not monotonic due to alloy fluctuations, while for holes this splitting remains nearly unchanged. For comparison, we show the *s-p* and *p-p* splittings for electrons (solid squares) and holes (open squares) in nonalloyed InAs/GaAs dots.

splitting is about 45 meV and depends weakly on height. On the other hand, for holes, this splitting changes from ≈ 20 to nearly 5 meV when height changes from 20 to 75 Å. Second, the *p-p* splitting shows the opposite behavior. Namely, for holes the magnitude of the splitting remains nearly constant at approximately 4 meV, and for electrons it changes nonmonotonically. It should be noted that the electronic *p-p* splitting is sensitive to alloy fluctuations and it can change by almost a factor of two by changing the alloy realization in the dot.⁴⁵

For comparison, *s-p* and *p-p* splittings in a lens-shaped, nonalloyed InAs/GaAs dots with $b = 252$ Å also appear in Fig. 5. The pure dot has a *s-p* splitting for holes that is nearly the same as in the $h = 35$ Å $\text{In}_{0.6}\text{Ga}_{0.4}\text{As}/\text{GaAs}$ dot, while this splitting for electrons is nearly 20% bigger and depends weakly on height. On the contrary, the *p-p* splitting for holes in the pure (nonalloyed InAs/GaAs) dot is about twice as big as in the $h = 35$ Å alloy dot, and for electrons the *p-p* splitting depends weakly on height and is similar in magnitude to the splittings in alloy dots. It should be noted that in pure (nonalloyed InAs/GaAs) dots the *hole* energy levels undergo a localization crossover (see discussion in Sec. III C) for tall dots, which render meaningless the notion of *s-p* and *p-p* splittings. (Such a localization crossover is absent for electrons.) For this reason, we have compared the splittings for the holes in a shallow ($h = 35$ Å) nonalloyed InAs/GaAs dot only while comparing the splitting for electrons in a range of heights.

B. Wave functions of confined states in $\text{In}_{0.6}\text{Ga}_{0.4}\text{As}/\text{GaAs}$ and nonalloyed InAs/GaAs dots: Mixed *s* and *p* character, and HH and LH character

Figure 6 compares the wave functions of LUMO (lowest electron) and HOMO (highest hole) states as a function of

height in $\text{In}_{0.6}\text{Ga}_{0.4}\text{As}/\text{GaAs}$ dots with base $b=252 \text{ \AA}$. To make the comparison, we plot isosurfaces that enclose 75% of the total charge density and show contour plots taken at 1 nm above the dot base. In addition, the s -orbital character of the LUMO and HOMO is indicated, so is the HOMO's heavy-hole and light-hole characters. Furthermore, for each height, the energy \mathcal{E}_0^e of LUMO is shown relative to $E_c(\text{GaAs})$ and the energy \mathcal{E}_0^h of HOMO relative to $E_v(\text{GaAs})$. Prominent results are the following. LUMO: The lateral spatial extent of the wave function depends weakly on height. On the contrary, as height decreases, the wave function extends into the barrier along the vertical direction. The s -orbital character of LUMO remains at nearly 90%. HOMO: Wave functions are more sensitive to height, showing a spatial extension that gets reduced significantly both in the lateral and vertical directions when height changes from 75 to 20 \AA . This reduction leads to a strong localization at the center of the dot for $h=20 \text{ \AA}$. The s -orbital character of the HOMO remains at about 90% up to $h=50 \text{ \AA}$; for taller dots the character of the HOMO becomes s and p mixed. This mixing reflects the reduction of the hole charge density near the center of the dot. The heavy-hole (HH) and light-hole (LH) characters also change with height in a similar manner as the s and p characters. Namely, for the three smaller dots (20, 35, and 50 \AA) the HOMO is mostly of the HH type, but as the height increases the LH character increases. We expect this behavior since the LH band offset increases within the dot as height increases. (See Fig. 3.)

Excited hole states

Figure 7 compares wave functions for excited hole states, namely, second (HOMO-1) and third (HOMO-2) hole states. As in Fig. 5, we show isosurfaces and contour plots, and present the orbital and HH/LH character of these states and the energies \mathcal{E}_1^h and \mathcal{E}_2^h for HOMO-1 and HOMO-2, respectively. The character of HOMO-1 and HOMO-2 are nearly the same at all heights. In addition, these states have a dominant p -orbital character for *all* heights regardless of the absence of p -shell structure for tall dots ($h=65$ and 75 \AA). (See Fig. 4.) As in the case of the HOMO state, the HOMO-1 and HOMO-2 states have an increasing light-hole character with increasing height. However, the percentage of the light-hole character is almost twice that of HOMO. For instance, at $h=75 \text{ \AA}$, the LH character of HOMO-2 is 17%, while the HOMO LH character is 11%.

C. Strain-driven hole localization

For dots containing both Ga and In ($\text{In}_{0.6}\text{Ga}_{0.4}\text{As}/\text{GaAs}$) with $b=252 \text{ \AA}$ and heights in the range of 20–75 \AA , we have shown that the wave functions of HOMO (\mathcal{E}_0^h) and HOMO-1 (\mathcal{E}_1^h), as well as other low-lying excited hole states, are localized inside the dot (see Figs. 6 and 7) and that these levels have a sizeable s - p splitting $\mathcal{E}_1^h - \mathcal{E}_0^h$ (see Fig. 5). On the contrary in lens-shaped, pure, nonalloyed InAs/GaAs quantum dots, localization of the low-lying hole states at the dot interface develops as the height of the dot increases. In addition, HOMO and HOMO-1 become nearly degenerate [e.g., $\mathcal{E}_0^h - E_v(\text{GaAs}) = 256.2 \text{ meV}$ and $\mathcal{E}_1^h - E_v(\text{GaAs})$

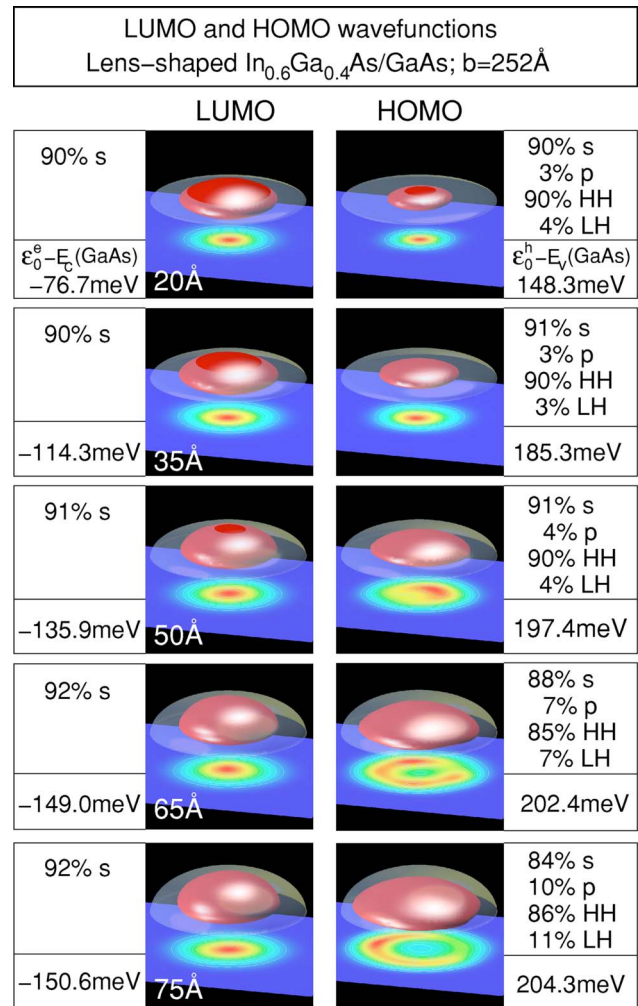


FIG. 6. (Color online) Height dependence of lowest electron level (LUMO) and highest hole level (HOMO) wave functions. Isosurfaces enclose 75% of the total charge density. Contours are taken at a plane 1 nm above the base. The energy relative to $E_c(\text{GaAs})$ and $E_v(\text{GaAs})$ is shown. The s - and p -orbital characters [see Eq. (7)] and the heavy-hole (HH) and light-hole (LH) characters are indicated. For the tallest dot, the wave functions are entirely confined within the dot, and the effective size of the dot—spatial extent of the wave functions—is nearly the same for LUMO and HOMO. For shorter dots the effective size gets significantly reduced for the HOMO, while it remains nearly unchanged for the LUMO.

$= 255.7 \text{ meV}$ at $h=75 \text{ \AA}$], so do HOMO-2 and HOMO-3. (It should also be noted that for the flat dot the energies of HOMO and HOMO-1 are bigger than in the alloy dot of the same size.) Remarkably, HOMO and HOMO-1 are *polarized* along $[1\bar{1}0]$ (Fig. 8), while HOMO-2 and HOMO-3 (not shown) are polarized along $[110]$. Figure 8 shows the development of this interfacial localization and the energies of HOMO and HOMO-1 relative to $E_v(\text{GaAs})$. As in Figs. 6 and 7, isosurfaces enclose 75% of the HOMO and HOMO-1 total charge density.

It should be noted that the pure nonalloyed InAs/GaAs dots have the *same* base size and *same* height range as the alloy dots we have previously discussed. Hence, hole localization does not have its origin in geometrical aspects of the quantum dots. Instead, the localization of the hole wave functions is driven by the biaxial strain present in the nanostructure (QD+GaAs matrix). To explain this result, we plot

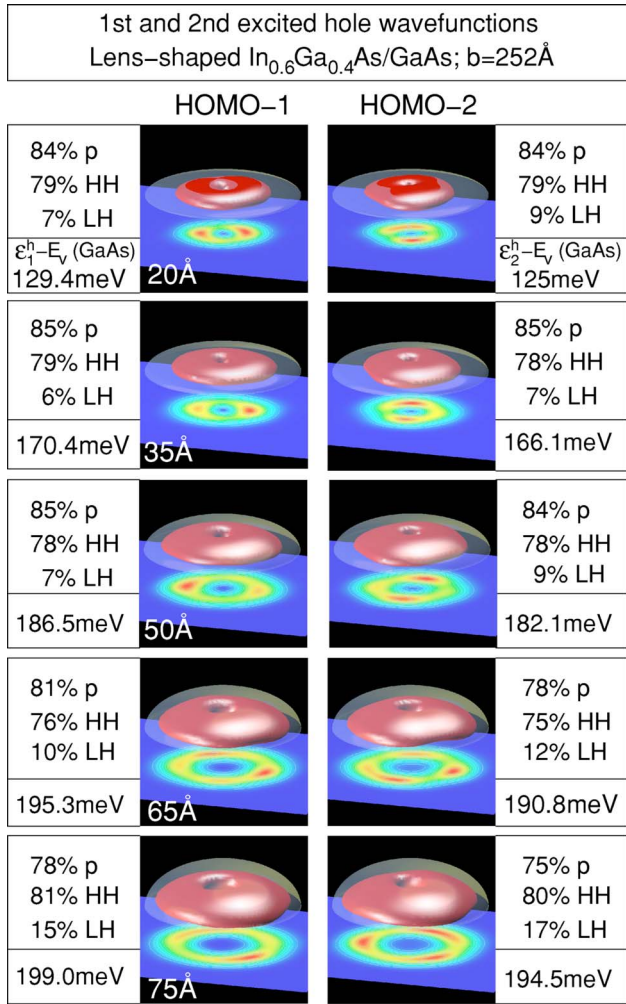


FIG. 7. (Color online) Wave functions of the first two excited hole levels HOMO-1 and HOMO-2 for different dot heights. As in Fig. 6, the isosurface encloses 75% of the total charge density and the contours are taken at 1 nm above the base. Labels indicate the p orbital character, the heavy-hole and light-hole characters, and the energy of the states relative to $E_v(\text{GaAs})$.

in Fig. 9(a) the valence-band offsets of heavy-hole (HH) and light-hole (LH) characters (inside the dot) along the line \vec{OO}' (see Figs. 1 and 3) and the energies of HOMO and HOMO-1 (thick dashes). In addition, we plot in Fig. 9(b) a three-dimensional rendering of the higher-energy hole band offset values at a plane normal to \vec{OO}' , cut slightly above the base of the dot. *First*, we see that as the dot height increases the pocket structure [indicated with arrows in Fig. 9(a)] that appears in the higher-energy band offset dramatically widens the confining potential (given by the band offset) along \vec{OO}' and that the band offset values decrease. Furthermore, the band offset becomes asymmetric, with the values at the top of the dot *smaller* than at the *base*. As a consequence, it becomes clear why the energies of the HOMO and HOMO-1 become bigger and we also expect the wave functions of these states to be localized near the base of the dot. It is important to mention that in the calculation of the energies of the HOMO and HOMO-1 we do not utilize the band offset we present in Fig. 9(a). *Second*, the band offsets shown in Fig. 9 present a “crown” structure at the dot-matrix interface.⁴⁶ This crown structure becomes more significant as

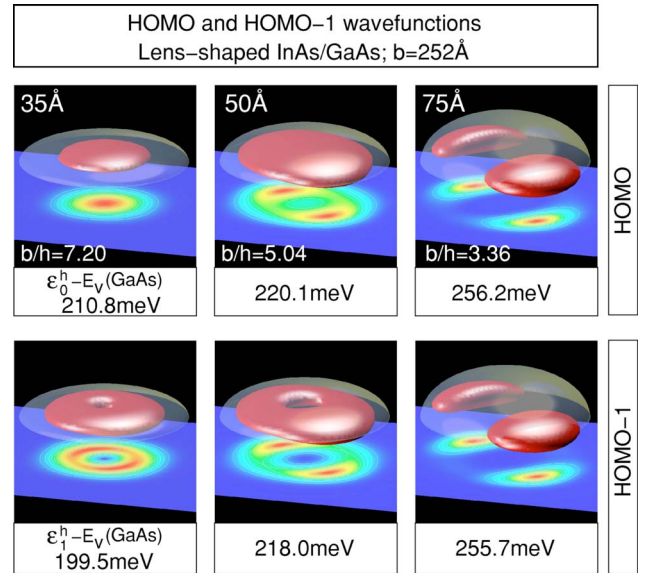


FIG. 8. (Color online) HOMO and HOMO-1 wave functions in pure, non-alloyed InAs/GaAs lens-shaped quantum dot as functions of height. The dots have the same base diameter $b=252\text{\AA}$. The aspect ratio b/h is shown, as well as the energy relative to $E_v(\text{GaAs})$. As before, the isosurfaces enclose 75% of the charge density and the contours are taken at 1 nm above the base. As height increases, interface localization takes place, and the HOMO and HOMO-1 become nearly degenerate.

height increases, as a consequence of the values of band offset along the $[110]$ and $[1\bar{1}0]$ directions presenting a weak dependence on height. *Finally*, the localization of the low-lying hole wave functions that develops as the height of pure, nonalloyed InAs/GaAs lens-shaped quantum dots increases is a result of the peculiar characteristics of the higher-energy valence-band offsets, which in turn are determined by the biaxial strain profile in the nanostructure.

Finally, it should be noticed that electron states do not experience interface localization; instead, they continue to form shells and the levels in these shells have a predominant, nonmixed orbital character (s, p, \dots). The reason for the absence of electron localization is that electron states are sensitive to the (hydrostatic) isotropic strain rather than to the biaxial strain.

D. Exciton transitions

Figure 10 shows the lowest bright transition (gap) of the exciton as a function of dot height, calculated at the single-particle (SP) level ($\mathcal{E}_0^e - \mathcal{E}_0^h$) and by using the many-body, configuration-interaction method.⁴² In the latter, we use a basis consisting of 12 electron and 20 hole confined levels ($n_e=12, n_h=20$) for heights $h=35-75\text{\AA}$ and ($n_e=6, n_h=20$) for $h=20\text{\AA}$. As expected, the transition energy decreases as height increases, due to confinement. However, the scaling with height differs significantly from predictions of single-band, effective mass ($\sim h^{-2}$).⁴⁷ Namely, by fitting our results for the height dependence of the gap to the function $a+b/h^\gamma$ we find $\gamma^{\text{SP}}=0.95$ and $\gamma^{\text{CI}}=1.09$. The value of the gap for large heights correspond, respectively, to $a^{\text{SP}}=1.117\text{ eV}$ and $a^{\text{CI}}=1.116\text{ eV}$ in the single-particle and CI approach. We expect the SP and CI scaling exponents to be different; as in the single-particle calculation the scaling is

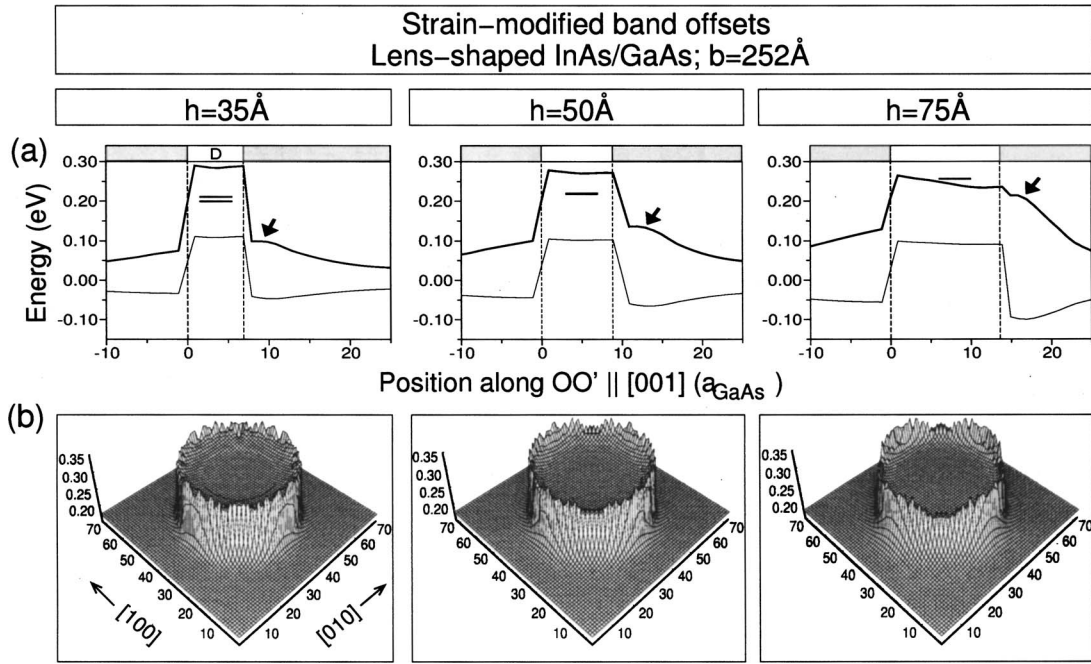


FIG. 9. Strain-modified band offsets in a pure, lens-shaped, nonalloyed InAs/GaAs quantum dot along the $\overline{OO'}$ direction (a) and in a plane normal to the latter cut at a height slightly above the base of the dot (b). Dashes in panel (a) correspond to the HOMO and HOMO-1 energy levels. The splitting among these levels decreases with the dot height. Arrows indicate pocket formation (see also Fig. 3) in the band offset due to strain accumulation at the dot-matrix interface at the top of the dot.

dictated by the scaling of the LUMO and HOMO, whereas in the CI calculation the electron-hole matrix elements are also included and the magnitude of these matrix elements decreases with height. The discrepancy between the scaling (γ) in single-band effective mass and both our SP and CI calculations can be attributed to nontrivial effects that are naturally accounted for within our atomistic approach, such as

nonparabolicity and multiband effects, and the position-dependent strain present in the nanostructure. The values of a at large heights is also expected to be different, and the difference is attributed to correlation effects that are present in the many-body, configuration-interaction approach. Thus, we expect a small difference (\sim meV) between a^{SP} and a^{CI} .

For comparison, we also present results for the lowest exciton transition [open (SP) and solid (CI) squares] in a lens-shaped, nonalloyed InAs/GaAs quantum dot. The values of the transition energies are smaller than in the alloy dots.

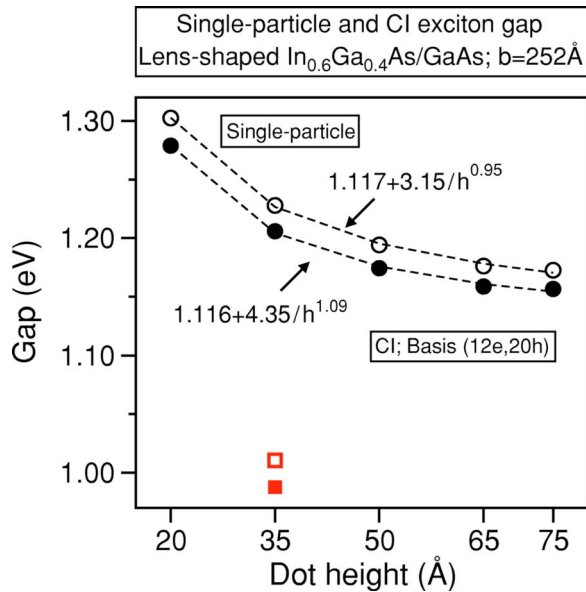


FIG. 10. (Color online) Exciton gap as a function of height. Single-particle (open circles) and configuration-interaction (CI, solid circles) results are shown. The CI basis is $(n_e=12, n_h=20)$ for $h=35-75$ Å and $(n_e=6, n_h=20)$ for $h=20$ Å. Dashed lines represent fits to the function $a+b/h^\gamma$. Fitting parameters are indicated. For comparison, we present results [open (SP) and solid (CI) squares] for a pure, nonalloyed InAs/GaAs dot.

IV. SUMMARY

By using a high-level atomistic approach, we have predicted spectroscopic characteristics of self-assembled $\text{In}_{1-x}\text{Ga}_x\text{As}/\text{GaAs}$ quantum dots as functions of height and composition. Several prominent features emerged.

(i) The biaxial strain at the dot-GaAs matrix interface increases with height, whereas, regardless of height, the strain is negligibly small along the $[011]$, $[01\bar{1}]$, and crystallographically equivalent directions.

(ii) Regardless of height and composition, the confined electron energy levels group in shells of nearly degenerate states. The average energy splitting among these shells depends weakly on height; however, this splitting is larger in pure, nonalloyed InAs/GaAs. In contrast, the confined hole energy levels form shells only in flat dots and near the highest hole level (HOMO).

(iii) In alloy dots, the *electrons'* s - p splitting depends weakly on height, while the p - p splitting depends nonmonotonically due to alloy fluctuations. In pure, nonalloyed InAs/GaAs dots, *both* these splittings depend weakly on

height. Further, the s - p splitting is larger while the p - p has nearly the same magnitude. For *hole* levels in alloy dots, the s - p splitting decreases with increasing height (the splitting in tall dots being about four times smaller than in flat dots), whereas the p - p splitting remains nearly unchanged. Shallow pure dots have an s - p splitting of nearly the same magnitude, whereas the p - p splitting is about three times larger.

(iv) As height increases, the s and p characters of the wave function of the HOMO becomes mixed, and so do the heavy-hole and light-hole characters.

(v) In alloy dots, regardless of height, the wave function of low-lying (near the HOMO) hole states are localized inside the dot. Remarkably, in pure, nonalloyed InAs/GaAs dots, as the dot height increases, these states become localized at the dot-matrix interface and are nearly degenerate. Furthermore, the localized states are polarized along $[1\bar{1}0]$ (HOMO and HOMO-1) and $[110]$ (HOMO-2 and HOMO-3). This localization effect is driven by the peculiarities of the biaxial strain present in the nanostructure.

(vi) The lowest exciton transition energy (gap) decreases with height, but the scaling (roughly $\sim h^{-1}$) differs significantly from the prediction of single-band effective mass ($\sim h^{-2}$).

The study we presented here may be used to bridge spectroscopy results with theory without the need for severe theoretical approximations.

ACKNOWLEDGMENTS

This work has been supported by U.S. DOE-SC-BES-DMS under Grant No. DE-AC36-99GO10337.

APPENDIX: CONVERGENCE

The LCBB method contains several convergence parameters: supercell size, number of bulk materials (M), number of bands (n), and number of \mathbf{k} points. The choice of bulk materials and number of bands can be physically motivated and justified, whereas the choice of supercell size and number of \mathbf{k} points is not as clear. For this reason, we conducted a convergence assessment on supercell size and number of \mathbf{k} points. As for the bulk materials, we choose (i) *unstrained* GaAs and (ii) InAs subject to strain values of $\varepsilon_{xx}=\varepsilon_{yy}=-0.06$ and $\varepsilon_{zz}=+0.04$. These values are typical of strain inside a nonalloyed InAs/GaAs lens-shaped quantum dot. For the bands n , when simulating the *electron* and *hole* energy levels we use, respectively, the lowest *conduction* band and the three highest *valence* bands of both bulk materials.

1. Supercell size

We consider cubic supercells of size $L_x \times L_y \times L_z$, where L_t ($t=x,y,z$) is measured in units of the lattice parameter of bulk GaAs a_{GaAs} . Based on strain calculations (see above), we selected a supercell size such that the strain profile within the quantum dot remained unchanged upon changing size. Nevertheless, it should be noted that although the strain may be converged within the dot the strain values at the boundary of the supercell may not be zero due to the slow relaxation of the strain fields. This residual strain introduces small changes ($\sim \text{meV}$) in the energy levels. For instance, Fig. 11 shows the effect of reducing the residual strain by changing the supercell size from $72 \times 72 \times 40$ to $72 \times 72 \times 48$ for a $h=20 \text{ \AA}$ dot.

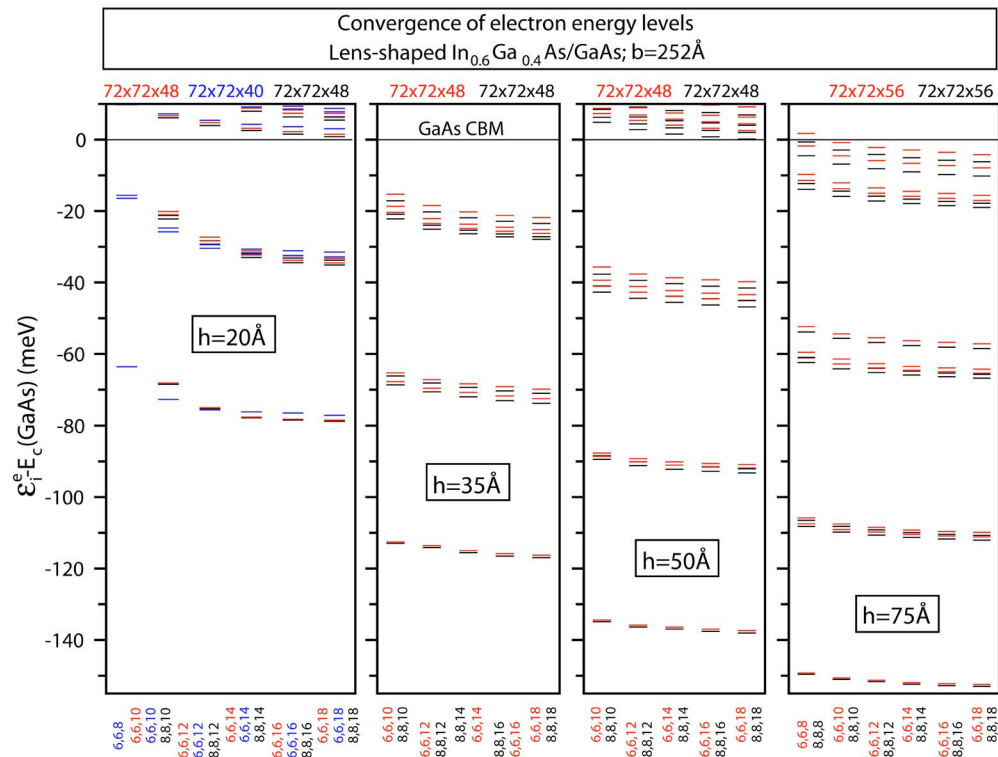


FIG. 11. (Color online) Convergence of the first 20 (including Kramers degeneracy) electron energy levels E_n^e of dots with different heights as a function of \mathbf{k} -point meshes and for different supercell sizes $[(L_x \times L_y \times L_z)]$. The results are color coded for clarity and are given with respect to GaAs CBM [$E_c(\text{GaAs}) = -4.093 \text{ eV}$]. The basis encompasses single-band Γ_{1c} GaAs and strained InAs bulk Bloch functions in the vicinity of the Γ point of the supercell. The threefold (Q, Q, K) represents the main-axis sizes of an ellipsoid in reciprocal space. This ellipsoid determines the number of \mathbf{k} points in the basis, which is the same for GaAs and InAs.

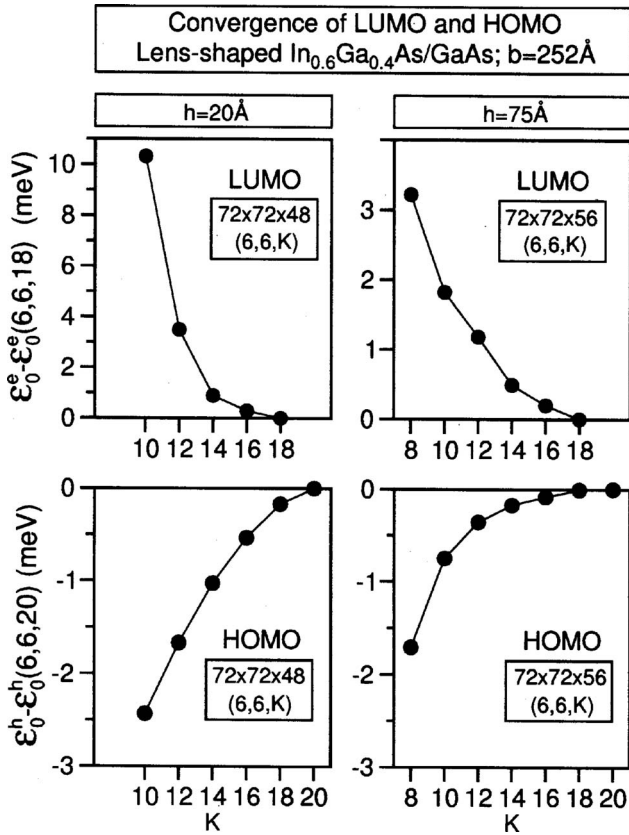


FIG. 12. Convergence of LUMO (\mathcal{E}_0^e) and HOMO (\mathcal{E}_0^h) energies relative to their value simulated with the highest number of \mathbf{k} points on a basis of the form $(6,6,K)$. To simulate the HOMO energy we include the three Γ_{15v} bands. The size of the supercell is indicated.

2. Number of \mathbf{k} points

The \mathbf{k} -point meshes enclose all the \mathbf{k} vectors around the Γ point that lie within an ellipsoid with main axes equal to $(2\pi/L_x)P$, $(2\pi/L_y)Q$, and $(2\pi/L_z)K$, respectively. P , Q , and K give the number of \mathbf{k} points taken along each Cartesian direction. In our convergence assessment $P=6,8$, $Q=P$, and K ranges from 8–18. Figure 11 shows the electron energy levels for several dots as a function of the \mathbf{k} -point meshes. We distinguish several features. (a) When compared with the energy of the levels, differences in energies are quicker to converge. (b) High-energy levels require larger \mathbf{k} -point meshes to converge within a given threshold. (c) The taller the quantum dots the smaller the number of \mathbf{k} points needed to converge. (d) The use of $(6,6,K)$ and $(8,8,K)$ \mathbf{k} -point meshes results in similar energies for the lowest electron level. The discrepancy between the predictions made with these two meshes increases for high-energy levels.

To present details of the convergence with respect to \mathbf{k} -point meshes, Fig. 12 shows a convergence assessment of HOMO and LUMO energies in flat ($h=20$ Å) and tall ($h=75$ Å) dots. The energy of HOMO converges visibly quicker than that of LUMO. This behavior holds for all hole energy levels and arises from the higher size (three Γ_{15v} bands) of the basis used in the simulation.

To summarize, the results we present in this work for each quantum dot derive from simulations with \mathbf{k} -point meshes that provide with energy levels converged within

TABLE I. Summary of supercell sizes $L_x \times L_y \times L_z$ (lengths in units of a_{GaAs}) and \mathbf{k} -point meshes (Q, Q, K) used in the simulations. Dots base $b=252$ Å. (c.f. Fig. 1 for dot geometry.)

Height (Å)	$L_x \times L_y \times L_z$	\mathbf{k} -point mesh
20	$72 \times 72 \times 48$	(6, 6, 13)
35	$72 \times 72 \times 48$	(6, 6, 13)
50	$72 \times 72 \times 48$	(6, 6, 12)
65	$72 \times 72 \times 48$	(6, 6, 12)
75	$72 \times 72 \times 56$	(6, 6, 10)

2 meV. Table I shows the supercell sizes and \mathbf{k} -point meshes we have used to simulate the electronic structure of each of the dots we have studied. It should be noted that *energy differences* are converged to much less than this lower bound.

- ¹S. Fafard, R. Leon, D. Leonard, J. L. Merz, and P. M. Petroff, Phys. Rev. B **52**, 5752 (1995); S. Fafard, D. Leonard, J. L. Merz, and P. M. Petroff, Appl. Phys. Lett. **65**, 1388 (1994); J.-Y. Marzin, J.-M. Gérard, A. Izraël, D. Barrier, and G. Bastard, Phys. Rev. Lett. **73**, 716 (1994); M. Grundmann *et al.*, Phys. Rev. Lett. **74**, 4043 (1994).
- ²F. Guffarth, R. Heitz, A. Schliwa, O. Stier, M. Geller, C. M. A. Kapteyn, R. Sellin, and D. Bimberg, Phys. Rev. B **67**, 235304 (2003); J. J. Finley *et al.*, Phys. Rev. B **63**, 073307 (2001); R. J. Warburton, C. S. Dürr, K. Karrai, J. P. Kotthaus, G. Medeiros-Ribeiro, and P. M. Petroff, Phys. Rev. Lett. **79**, 5282 (1997).
- ³J. J. Finley, Phys. Rev. B **63**, 161305 (2001).
- ⁴M. Bayer, O. Stern, P. Hawrylak, S. Fafard, and A. Forchel, Nature (London) **405**, 923 (2000); E. Dekel, D. Gershoni, E. Ehrenfreund, J. M. Garcia, and P. Petroff, Phys. Rev. B **61**, 11009 (2000); F. Findeis, A. Zrenner, G. Böhm, and G. Abstreiter, Solid State Commun. **114**, 227 (2000); L. Landin, M. S. Miller, M.-E. Pistol, C. E. Pryor, and L. Samuelson, Science **280**, 262 (1998); M. Bayer, T. Gutbrod, A. Forchel, V. D. Kulakovskii, A. Gorbunov, M. Michel, R. Steffen, and K. H. Wang, Phys. Rev. B **58**, 4740 (1998).
- ⁵E. Dekel, D. Gershoni, E. Ehrenfreund, D. Spektor, J. M. Garcia, and P. M. Petroff, Phys. Rev. Lett. **80**, 4991 (1998).
- ⁶B. Urbaszek, R. J. Warburton, K. Karrai, B. D. Gerardot, P. M. Petroff, and J. M. Garcia, Phys. Rev. Lett. **90**, 247403 (2003); M. Bayer *et al.*, Phys. Rev. B **65**, 195315 (2002); J. J. Finley, D. J. Mowbray, M. S. Skolnick, A. S. Ashmore, C. Baker, A. F. G. Monte, and M. Hopkinson, Phys. Rev. B **66**, 153316 (2002).
- ⁷A. Zunger, Phys. Status Solidi A **190**, 467 (2002).
- ⁸L. He, G. Bester, and A. Zunger, Phys. Rev. B **70**, 235316 (2004).
- ⁹G. Bester, S. Nair, and A. Zunger, Phys. Rev. B **67**, 161306 (2003).
- ¹⁰G. Bester and A. Zunger, Phys. Rev. B **68**, 073309 (2003).
- ¹¹J. Simonin, C. R. Proetto, Z. Barticevic, and G. Fuster, Phys. Rev. B **70**, 205305 (2004).
- ¹²A. Wojs, P. Hawrylak, S. Fafard, and L. Jacak, Phys. Rev. B **54**, 5604 (1996).
- ¹³J. Shumway, A. J. Williamson, A. Zunger, A. Passaseo, M. DeGiorgi, R. Cingolani, M. Catalano, and P. Crozier, Phys. Rev. B **64**, 125302 (2001).
- ¹⁴A. J. Williamson, L. W. Wang, and A. Zunger, Phys. Rev. B **62**, 12963 (2000).
- ¹⁵N. Liu, H. K. Lyo, C. K. Shih, M. Oshima, T. Mano, and N. Koguchi, Appl. Phys. Lett. **80**, 4345 (2002).
- ¹⁶D. M. Bruls, J. W. A. M. Vugs, P. M. Koenraad, H. W. M. Salemik, J. H. Wolter, M. Hopkinson, M. S. Skolnick, F. Long, and S. P. A. Gill, Appl. Phys. Lett. **81**, 1708 (2002).
- ¹⁷Q. Gong, P. Offeremans, R. Nötzel, P. M. Koenraad, and J. H. Wolter, Appl. Phys. Lett. **85**, 5697 (2004).
- ¹⁸L. Jacak, P. Hawrylak, and A. Wojs, *Quantum Dots* (Springer, Berlin, 1997).
- ¹⁹M. A. Cusak, P. R. Briddon, and M. Jaros, Phys. Rev. B **54**, R2300 (1996); J. Marzin and G. Bastard, Solid State Commun. **92**, 437 (1994).
- ²⁰C. Pryor, Phys. Rev. B **57**, 7190 (1998); T. B. Bahder, Phys. Rev. B **45**, 1629 (1992); T. B. Bahder, Phys. Rev. B **41**, 11992 (1990); [see also T. B. Bahder, Phys. Rev. B **46**, 9913 (1992)], and references therein.
- ²¹L.-W. Wang and A. Zunger, Phys. Rev. B **59**, 15806 (1999).

- ²²L. W. Wang, A. J. Williamson, A. Zunger, H. Jiang, and J. Singh, *Appl. Phys. Lett.* **76**, 339 (2000).
- ²³A. Zunger, *Phys. Status Solidi B* **224**, 727 (2001).
- ²⁴S. Lee, O. L. Lazarenkova, P. von Allmen, F. Oyafuso, and G. Klimeck, *Phys. Rev. B* **70**, 125307 (2004); R. Santoprete, B. Koiler, R. B. Capaz, P. Kratzer, Q. K. Liu, and M. Scheffler, *Phys. Rev. B* **68**, 235311 (2003); G. W. Bryant and W. Jaskólski, *Phys. Rev. B* **67**, 205320 (2003); S. Lee, L. Jönsson, J. W. Wilkins, G. W. Bryant, and G. Klimeck, *Phys. Rev. B* **63**, 195318 (2001); K. Leung and K. B. Whaley, *Phys. Rev. B* **56**, 7455 (1997).
- ²⁵R. Ferreira, *Physica E (Amsterdam)* **13**, 216 (2002).
- ²⁶M. Grundmann, O. Stier, and D. Bimberg, *Phys. Rev. B* **52**, 11969 (1995).
- ²⁷O. Stier, M. Grundmann, and D. Bimberg, *Phys. Rev. B* **59**, 5688 (1999).
- ²⁸F. Guffarth, R. Heitz, A. Schliwa, O. Stier, N. N. Ledentsov, A. R. Kovsh, V. M. Ustinov, and D. Bimberg, *Phys. Rev. B* **64**, 085305 (2001).
- ²⁹C. Pryor, *Phys. Rev. B* **60**, 2869 (1999).
- ³⁰R. Heitz, S. Rodt, A. Schliwa, and D. Bimberg, *Phys. Status Solidi B* **238**, 273 (2003); O. Stier, R. Heitz, A. Schliwa, and D. Bimberg, *Phys. Status Solidi A* **190**, 477 (2002).
- ³¹J. Kim, L. W. Wang, and A. Zunger, *Phys. Rev. B* **57**, R9408 (1998).
- ³²D. Leonard, M. Krishnamurthy, C. M. Reaves, S. P. Denbaars, and P. M. Petroff, *Appl. Phys. Lett.* **63**, 3203 (1993); D. Leonard, K. Pond, and P. M. Petroff, *Phys. Rev. B* **50**, 11687 (1994); S. Raymond, S. Fafard, P. J. Poole, A. Wojs, P. Hawrylak, S. Charbonneau, D. Leonard, R. Leon, P. M. Petroff, and J. L. Merz, *Phys. Rev. B* **54**, 11548 (1996); Z. R. Wasilewski, S. Fafard, and J. P. McCaffrey, *J. Cryst. Growth* **201–202**, 1131 (1999); A. G. Cullis, D. J. Norris, T. Walther, M. A. Migliorato, and M. Hopkinson, *Phys. Rev. B* **66**, 081305 (2002); S. Anders, C. S. Kim, B. Klein, M. W. Weller, and R. P. Mirin, *Phys. Rev. B* **66**, 125309 (2002).
- ³³M. Tadić, F. M. Peeters, K. L. Janssens, M. Korkusinski, and P. Hawrylak, *J. Appl. Phys.* **92**, 5819 (2002).
- ³⁴C. Pryor, J. Kim, L. W. Wang, A. J. Williamson, and A. Zunger, *J. Appl. Phys.* **83**, 2548 (1998).
- ³⁵R. M. Martin, *Phys. Rev. B* **1**, 4005 (1970); P. N. Keating, *Phys. Rev.* **145**, 637 (1966).
- ³⁶G. Bester and A. Zunger, *Phys. Rev. B* **71**, 045318 (2005).
- ³⁷W. Sheng and J.-P. Leburton, *Phys. Status Solidi B* **237**, 394 (2003); O. Stier, *Electronic and Optical Properties of Quantum Dots and Wires* (Wissenschaft & Technik, Berlin, 2001).
- ³⁸C. Pryor, M.-E. Pistol, and L. Samuelson, *Phys. Rev. B* **56**, 10404 (1997).
- ³⁹O. L. Lazarenkova, P. von Almen, F. Oyafuso, S. Lee, and G. Klimeck, *Appl. Phys. Lett.* **85**, 4193 (2004).
- ⁴⁰J. D. Eshelby, *J. Appl. Phys.* **25**, 255 (1954).
- ⁴¹S.-H. Wei and A. Zunger, *Phys. Rev. B* **49**, 14337 (1994).
- ⁴²This shell-structure feature agrees qualitatively with the prediction of a single-band, effective-mass, two-dimensional harmonic oscillator (see Ref. 18).
- ⁴³A. Franceschetti, H. Fu, L. W. Wang, and A. Zunger, *Phys. Rev. B* **60**, 1819 (1999).
- ⁴⁴R. Resta, *Phys. Rev. B* **16**, 2717 (1977).
- ⁴⁵G. A. Narvaez, G. Bester, and A. Zunger (unpublished).
- ⁴⁶This “crown” structure has been predicted by He and co-workers in Ref. 8 and has been argued that it is this structure that is responsible for similar localization of hole wave functions found in large, nonalloyed InAs/GaAs spherical quantum dots. (Ref. 8).
- ⁴⁷For single-band effective-mass calculations of the single-particle electronic levels in lens-shaped semiconductor quantum dots with aspect ratio $h/b=0.25$ and 0.5 see J. Even and S. Loualiche, *J. Phys. A* **36**, 11677 (2003) and A. H. Rodriguez, C. Trallero-Giner, S. E. Ulloa, and J. Marín-Antuña, *Phys. Rev. B* **63**, 125319 (2001), respectively.